AGU PUBLICATIONS

JGR

Journal of Geophysical Research: Atmospheres

RESEARCH ARTICLE
10.1002/2017JD027157

Key Points:
- We present a streamer model with electromagnetic propagation, electron transport, impact ionization, attachment, and photoionization
- The radiated field of a corona is likely dominated in the UHF range by the electromagnetic pulses emitted by streamer collisions
- The electric field that, after a streamer collision, penetrates into each streamer is capable of accelerating electrons up to 100 keV

Supporting Information:
- Supporting Information S1
- Data Set S1

Correspondence to:
A. Luque,
aluque@iaa.es

Citation:
Luque, A. (2017). Radio frequency electromagnetic radiation from streamer collisions. *Journal of Geophysical Research: Atmospheres*, *122*, 10,497–10,509. https://doi.org/10.1002/2017JD027157

Received 17 MAY 2017
Accepted 13 SEP 2017
Accepted article online 20 SEP 2017
Published online 12 OCT 2017

Radio Frequency Electromagnetic Radiation From Streamer Collisions

Alejandro Luque

[1] Instituto de Astrofísica de Andalucía (IAA), CSIC, Granada, Spain

Abstract We present a full electromagnetic model of streamer propagation where the Maxwell equations are solved self-consistently together with electron transport and reactions including photoionization. We apply this model to the collision of counter-propagating streamers in gaps tens of centimeters wide and with large potential differences of hundreds of kilovolts. Our results show that streamer collisions emit electromagnetic pulses that, at atmospheric pressure, dominate the radio frequency spectrum of an extended corona in the range from about 100 MHz to a few gigahertz. We also investigate the fast penetration, after a collision, of electromagnetic fields into the streamer heads and show that these fields are capable of accelerating electrons up to about 100 keV. By substantiating the link between X-rays and high-frequency radio emissions and by describing a mechanism for the early acceleration of runaway electrons, our results support the hypothesis that streamer collisions are essential precursors of high-energy processes in electric discharges.

Plain Language Summary Long electric discharges such as a lightning stroke simultaneously produce bursts of X-rays and radio frequency noise. Here we present a numerical model that explains this coincidence by attributing both phenomena to the collisions of counter-propagating conducting filaments called "streamers."

1. Introduction

In a long air gap, a high electric potential applied to a pointed electrode initiates an electric discharge which, in its earliest phase, consists of tens or hundreds of thin filaments called streamers. These are ionized channels that progress toward the opposite electrode due to strong impact ionization in their tips. When both electrodes in a discharge are pointed enough, they launch streamers of opposite polarities that collide within the gap, closing a conducting path between the two extremes. Streamer collisions also occur during the progression of a stepped leader, where a corona that emanates from the main leader channel collides with streamers of opposite polarity that emerge from a space stem.

Streamer encounters have received considerable attention due to their possible link to the emission of X-rays from electric discharges and lightning. As streamers are relatively efficient electrical conductors, in a head-on collision, the potential difference between the streamer tips is a large fraction of the potential difference between the electrodes. Just before the collision, this potential difference is compressed within the short distance between the two tips and produces extremely high but localized electric fields. Cooray et al. (2009) hypothesized that these fields exceed the so-called thermal runaway threshold (about 260 kV/cm at atmospheric pressure, Moss et al., 2006), which enables electrons to be accelerated from energies around 1 eV to energies above 1 keV where the air friction decreases and electrons runaway. These electrons, upon a collision with a nucleus, emit X-ray photons as detected around long discharges (Dwyer et al., 2005; Kochkin et al., 2012, 2015; Montanyà et al., 2015; Nguyen et al., 2008, 2010; Rahman et al., 2008) and lightning leaders (Dwyer et al., 2011; Moore et al., 2001). This hypothesis is supported by laboratory measurements where the time of X-ray emissions coincides with the time of approach of counter-propagating streamers (Kochkin et al., 2012, 2015; Østgaard et al., 2016). Recent simulations by Ihaddadene and Celestin (2015) and Köhn et al. (2017) confirm that the electric field in a streamer collision exceeds the thermal runaway threshold but these authors estimate the time scale of the field peak at around 10^{-11} s, which they claim is too fast to produce the detected X-ray signals because not enough electrons are accelerated to high energies. We note, however, that in these works the gap length is of the order of 1 cm and the total available potential is of the order of a few tens of kilovolt, far below the voltage of about 1 MV often reached in experiments.

On the other hand, the emission of X-rays in a long spark has been recently correlated with radio frequency radiation in the UHF range (Montanyà et al., 2015). Previously, Petersen and Beasley (2014) detected this radiation close to lightning stepped leaders. Given the fast depletion of the electric field immediately following a streamer collision, one expects the emission of a strong high-frequency electromagnetic pulse from each streamer encounter. However, detailed calculations of such pulses are, as far as we know, missing from the literature.

Here we address this topic with a full electromagnetic streamer model that resolves the smallest temporal scales involved in a streamer collision. This work is the first application of a new streamer simulation code that combines a high-order conservative discretization for electron transport with a finite difference, time domain (FDTD) scheme for the evolution of the electromagnetic fields. Previous streamer models compute electric fields within the quasi-electrostatic approximation, which is valid as long as the electromagnetic wavelength associated with the characteristic time scale of the problem is much longer than the system size. But, as we mentioned above, the time scale of a streamer head-on collision can be as short as 10^{-11} s and in this time light propagates about 3 mm, which is comparable to or smaller than the size of a streamer. Therefore, an accurate investigation of the dynamics of streamer collisions requires a full electromagnetic calculation.

Although accounting for electromagnetic wave propagation involves some computational cost, the burden is not as heavy as might be thought. Generally, a streamer simulation implies using time steps $\Delta t \approx \Delta x/v$, where Δx is the size of the spatial grid and v is the speed at which information propagates in the model. In a purely hyperbolical system of partial differential equations this speed is the maximum speed of particles or waves present in the model. In a streamer this would be the velocity of electrons, around 10^5 m/s. However, traditional streamer models are based on the solution of the Poisson equation which, due to its nonlocal nature, implies instantaneous propagation of information. That means that using the electron velocity to define the time step Δt is not enough to ensure stability. A more realistic choice for the speed of information in the model is the velocity of a streamer, a few times 10^6 m/s. Since an electromagnetic simulation requires time steps of roughly $\Delta t \approx \Delta x/c$, it performs about 100 times more time steps than quasi-static simulations.

On the other hand an electromagnetic simulation provides two distinct advantages that in part compensate that factor of 100. First, the Maxwell equations are purely local and therefore time domain numerical schemes such as FDTD are easily parallelizable (to be updated, a grid cell needs information only about immediately adjacent grid cells), scaling close to linearly up to arbitrarily large grid sizes. The nonlocality of the Poisson equation makes it harder to parallelize; although parallel solvers exist based on multigrid (Teunissen & Ebert, 2017) or Krylov space methods, they involve more communication between the computational nodes and therefore do not scale as well. The second advantage of electromagnetic solvers concerns the domain size. Perfectly matched layers (PML), introduced to FDTD schemes by Berenger (1994), drastically reduce, at a small cost, the required domain size of a streamer simulation, restricting it to only the streamer and a narrow region around it. As modern PML implementations almost perfectly filter out the reflection of waves back into the simulation domain, the numerical artifacts introduced by these boundaries are negligible. For electrostatic codes, a similar narrowing of the computational domain involves a significant cost, although efficient methods exist that increase only by a factor of 2 the amount of work required to solve the Poisson equation (Malagón-Romero & Luque, 2017). Due to these two factors, full electromagnetic simulations of streamers are, if not comparable in efficiency to traditional quasi-electrostatic codes, at least practical and capable of performing streamer simulations within a reasonable time.

In the following sections we first discuss the details of our model and its implementation, subsequently applying it to simulations of streamer collisions. We then quantify the electromagnetic radiation emanating from each of these encounters and the fast penetration of electric fields into the streamer bodies immediately after the collision. We then discuss the implications of our results for the emissions of X-rays from long sparks and leaders. We finish with a short summary and some conclusions.

2. Model

Our model solves the complete Maxwell equations which, given appropriate initial conditions, reduce to the two curl equations:

$$\epsilon_0 \frac{\partial \mathbf{E}}{\partial t} = \nabla \times \mathbf{H} - \mathbf{J}, \tag{1a}$$

$$\mu_0 \frac{\partial \mathbf{H}}{\partial t} = -\nabla \times \mathbf{E}, \tag{1b}$$

where **E** and **H** are the electric and magnetic fields, **J** is the electric current density, and ϵ_0 and μ_0 are the electric permittivity and magnetic permeability of vacuum.

Equations (1a) and (1b) are coupled to the conservation equation for electrons. We consider that within our time scales, only electrons are mobile and thus the electric current density **J** derives from the electron flux Γ_e as $\mathbf{J} = -e\Gamma_e$, where e is the elementary charge. This flux includes drift and diffusion, yielding

$$\Gamma_e = -n_e \mu \mathbf{E} - D\nabla n_e, \tag{2}$$

where n_e is the electron number density, μ is the electron mobility, and D is the electron diffusion coefficient. Strictly speaking, the diffusion current does not respect the relativistic speed limit of c; however, in our case this term is negligible almost everywhere, its effect being restricted to smoothing the high-gradient areas around a streamer head. For reasons to be discussed below our scheme is limited to constant electron mobility and diffusion coefficient. The validity of this approximation is discussed in the supporting information. In this work $\mu = 372\ \mathrm{cm^2V^{-1}s^{-1}}$, $D = 1.8 \times 10^3\ \mathrm{cm^2s^{-1}}$ (see, e.g., Davies et al., 1971).

The conservation equation for electrons reads

$$\frac{\partial n_e}{\partial t} = -\nabla \cdot \Gamma_e + S, \tag{3}$$

where S is the net production of free electrons. Here we consider three contributions to S: impact ionization, dissociative attachment, and photoionization. We have

$$S = \nu_i n_e - \nu_a n_e + S_{\mathrm{ph}} = \nu_{\mathrm{eff}} n_e + S_{\mathrm{ph}}, \tag{4}$$

where ν_i and ν_a are, respectively, the impact ionization and the dissociative attachment rates. We approximate them as functions of the local electric field using the Townsend approximation,

$$\nu_{i,a} = \mu |E_{i,a}| \alpha_{i,a} \exp(-|E_{i,a}|/E), \tag{5}$$

where $\alpha_{i,a}$ and $E_{i,a}$ are the same as those listed (Luque & Ebert, 2009).

The photoionization term in (4) stands for the ionization of oxygen due to ultraviolet radiation emitted by molecular nitrogen states excited in the high-field region of a streamer. This process is essential for the propagation of positive (cathode-directed) streamers and plays a significant role in the propagation of negative streamers (Luque et al., 2008; Wormeester et al., 2010). Determining the rate of photoionization is computationally expensive, and several methods have been proposed to simplify and speed up its calculation (Bourdon et al., 2007; Luque et al., 2007; Ségur et al., 2006). These approaches assume an instantaneous travel of photons from the active volume in the streamer's head to the point where the photon ionizes an oxygen molecule. Here since we are resolving time scales up to the propagation time of electromagnetic waves, we also have to consider the propagation of photoionizing radiation. Solving the full radiative transport equation would impose excessive memory and computing requirements so we opted for reducing this equation using the three-group Eddington approximation, discussed by Ségur et al. (2006) and Bourdon et al. (2007). But, in contrast to these previous works, we do not neglect the transient term.

Within this approximation we consider that the frequency dependence of the photon distribution function can be reduced to three components indexed by $j = 1, 2, 3$. This reduces the full dependence with wavelength of the absorption length into only three lengths that are chosen to fit as closely as possible the expression derived by Zhelezniak et al. (1982). Each of these components is described by a radiation field $\Psi_j(\mathbf{r}, \mathbf{\Omega}, t)$ that depends on position **r**, angular direction $\mathbf{\Omega}$, and time t. In principle each of these fields satisfies an effective monochromatic radiative transport equation

$$\frac{\partial \Psi_j}{\partial t} + c\mathbf{\Omega} \cdot \nabla \Psi_j + c\lambda_j \Psi_j = \frac{I}{4\pi}, \tag{6}$$

where λ_j is the absorption coefficient of component j and I is the source of ionizing photons at a given location. Note that we deviate slightly from the notation of Bourdon et al. (2007) by using a density-dependent absorption rate instead of explicitly multiplying by the oxygen partial pressure. Following Zhelezniak et al. (1982),

we approximate I as proportional to the impact ionization source and incorporate into it the photoionization efficiency factor ξ and the collisional deactivation (quenching) factor:

$$I = \frac{p_q}{p + p_q} \kappa \xi \nu_i n_e, \tag{7}$$

where p_q is the quenching pressure of the nitrogen states that emit photoionizing radiation ($p_q \approx 0.08$ bar, Legler, 1963), κ is the average number of excitations of these states for each electron impact ionization, and ξ is the probability that a photon ionizes an oxygen molecule. We used $\kappa\xi = 0.06$ (Ségur et al., 2006).

In the Eddington approximation we expand the angular dependence of Ψ_j into spherical harmonics, keeping only the first-order term

$$\Psi_j(\mathbf{r}, \mathbf{\Omega}, t) = \frac{1}{4\pi}\Psi_{0,j}(\mathbf{r}, t) + \frac{3}{4\pi}\mathbf{\Omega} \cdot \mathbf{\Psi}_{1,j}(\mathbf{r}, t). \tag{8}$$

As mentioned by Ségur et al. (2006), the validity of this approximation rests on the fact that the absorption length of the photoionizing radiation is longer than the characteristic length scales of the streamer heads. Bourdon et al. (2007) checked that the three-group Eddington approximation is accurate for streamer simulations.

After some algebraic manipulations equation (8) leads to coupled equations for the isotropic field $\Psi_{0,j}$ and the first-order anisotropic field $\mathbf{\Psi}_{1,j}$:

$$\frac{\partial \Psi_{0,j}}{\partial t} = I - c\lambda_j \Psi_{0,j} - c\nabla \cdot \mathbf{\Psi}_{1,j}, \tag{9a}$$

$$\frac{a}{b}\partial \mathbf{\Psi}_{1,j} \partial t = -c\lambda_j \mathbf{\Psi}_{1,j} - \frac{c}{3}\nabla \Psi_{0,j}. \tag{9b}$$

The total density of photoionization events can be calculated from the isotropic component of the radiation field as

$$S_{\text{ph}} = \sum_j A_j \Psi_{0,j}. \tag{10}$$

We obtained the weights A_j and the absorption coefficients λ_j from the fit provided by Bourdon et al. (2007) (Table 3).

We note that, by assuming an angular dependency with limited validity, the Eddington approximation (8) imposes some distortions to the propagation of photons. Combining (9a) and (9b) in vacuum ($I = 0$, $\lambda_j = 0$), we obtain the wave equation $\partial_t^2 \Psi_{0,j} = c^2 \nabla^2 \Psi_{0,j}/3$, which implies that the photoionization field propagates at a speed $c/\sqrt{3}$ instead of c, as would be expected. Furthermore, within the Eddington approximation the photoionizing radiation of several streamers does not add linearly but instead interact and may cause unphysical artifacts. However, as photoionization is only relevant in a small volume surrounding each streamer head, and once two streamers are in close proximity impact ionization dominates over photoionization, we consider these artifacts to have a negligible effect in our simulations. Although costly, higher-order expansions of the radiative transfer equation are desirable in order to mitigate these problems.

3. Numerical Implementation

Our numerical implementation combines a classical FDTD discretization for the Maxwell equations (Inan & Marshall, 2011; Taflove & Hagness, 2005) and a conservative finite volume method for electron transport.

The FDTD scheme is based on a standard Yee grid and time stepping (Yee, 1966), as shown in Figure 1. The locations where we evaluate the two components of the electric field make it natural to evaluate the divergence of this field at the cell centers, which is where we have located the values of the electron density. To integrate the electron transport equation (3), we need the electron flux (or, equivalently, the electric current density) at the cell interfaces. The sharp gradient of the electron density in a streamer front demands high-order, flux-limited discretization schemes.

Here we will adapt the discretization employed by Montijn et al. (2006). We describe our scheme particularized to the transport in the z direction; the expressions for the r-directed flux are analogous. We first divide the z-directed flux between cells (i, j) and $(i, j + 1)$ into its advective and diffusive components,

$$\Gamma_{z,(i,j+1/2)} = \Gamma^a_{z,(i,j+1/2)} + \Gamma^d_{z,(i,j+1/2)}. \tag{11}$$

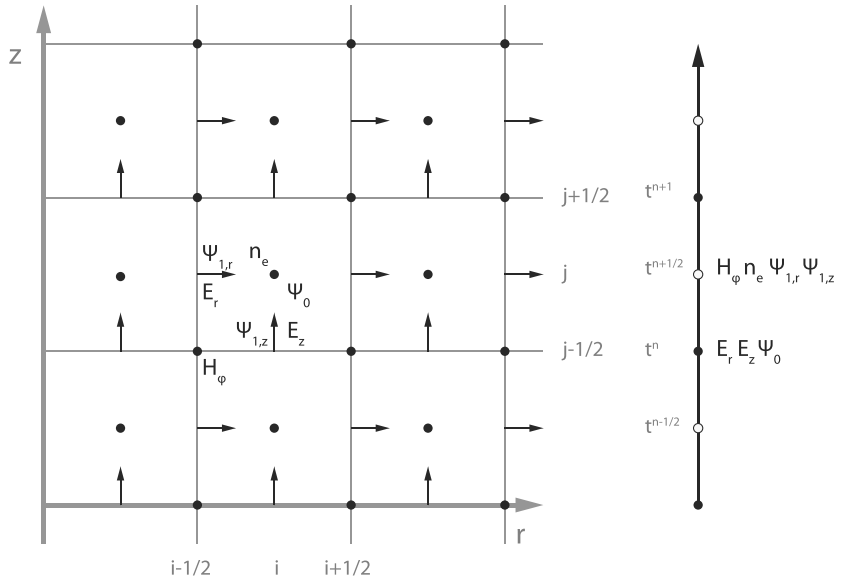

Figure 1. (left) Grid locations of all our simulation variables. The three components of the transversal magnetic mode of the electromagnetic field are located in a standard Yee grid. The two components of the anisotropic, first-order component of the photoionization field are colocated with the respective components of the electric field. The electron density and the isotropic component of the photoionization field are located at cell centers. (right) Time evaluation of all the variables. Again, we follow the conventional evaluation times for electromagnetic fields in FDTD schemes. The isotropic photoionization component coincides with evaluations of the electric field, whereas the electron density and the anisotropic photoionization coincide with the magnetic field.

The advective part is discretized as

$$\begin{aligned}\Gamma^a_{z,(i,j+1/2)} = &-\mu E^-_{z,(i,j+1/2)}\left[n_{e,(i,j)} + \psi(\theta_{(i,j)})(n_{e,(i,j+1)} - n_{e,(i,j)})\right] \\ &-\mu E^+_{z,(i,j+1/2)}\left[n_{e,(i,j+1)} + \psi\left(\theta^{-1}_{(i,j+1)}\right)(n_{e,(i,j)} - n_{e,(i,j+1)})\right],\end{aligned} \tag{12}$$

where $E^+ = \max(E, 0)$, $E^- = \min(E, 0)$,

$$\theta_{(i,j+1)} = \frac{n_{e,(i,j)} - n_{e,(i,j-1)}}{n_{e,(i,j+1)} - n_{e,(i,j)}}, \tag{13}$$

and $\psi(\cdot)$ is a flux limiter, which we take to be the Koren limiter

$$\psi(\theta) = \max\left(0, \min\left(1, \frac{1}{3} + \frac{\theta}{6}, \theta\right)\right). \tag{14}$$

The diffusive flux, on the other hand, reads

$$\Gamma^d_{z,(i,j+1/2)} = \frac{D}{\Delta z}\left(n_{e,(i,j)} - n_{e,(i,j+1)}\right), \tag{15}$$

with Δz being the grid spacing in the z direction.

This scheme must be incorporated into the FDTD evolution equation for the electric field, which is a first-order discretization of (1a). Following the standard approach in FDTD methods, we update the electric field from time t^n to time t^{n+1} provided magnetic field and electron densities at time $t^{n+1/2}$. Interpolating the current density, we arrive at this finite difference equation for the z component of the electric field:

$$\epsilon_0 \frac{E_z|^{n+1} - E_z|^n}{\Delta t} = \nabla \times H|^{n+1/2}_z - \frac{J_z|^{n+1} + J_z|^n}{2}. \tag{16}$$

To avoid cluttering, we omit the standard discretization of the term $\nabla \times H|_z^{n+1/2}$ and we drop the grid subindices $(i, j + 1/2)$. Decomposing J_z into advective and diffusive parts, $J_z^a = -e\Gamma^a$, $J_z^d = -e\Gamma^d$, and rearranging terms, we arrive at

$$E_z|^{n+1} + \frac{\Delta t J_z^a|^{n+1}}{2\epsilon_0} = E_z|^n - \frac{\Delta t J_z^a|^n}{2\epsilon_0} + \nabla \times H|_z^{n+1/2} - \frac{\Delta t J_z^d|^{n+1/2}}{\epsilon_0}, \tag{17}$$

where we took into account that J^d depends only on the electron densities and not on the electric field and therefore to first order $J_z^d|^n = J_z^d|^{n+1} = J_z^d|^{n+1/2}$ in the interval (t^n, t^{n+1}).

In the update step for E_z the right-hand side of equation (17) is known. The left-hand side is a monotonically increasing function of $E_z|^{n+1}$ which can be inverted easily. Indeed, the sign of $E_z|^{n+1}$ is the same as that of the right-hand side of equation (17) so it determines which of the terms in (12) applies; once this is set, one can write $J_z^a|^{n+1} = \sigma|^{n+1} E_z|^{n+1}$ and from (17) find $E_z|^{n+1}$.

This update scheme is valid only for a constant mobility and diffusion constant. If these parameters depend on the local electric field, the absolute value of the electric field appears in (17) and couples E_z with E_r, which are evaluated at different locations. In that case (17) turns into a system of coupled nonlinear equations with about as many unknowns as grid points. To avoid this massive complication, we assumed a constant electron mobility and diffusion constant.

Turning now to photoionization, the set of equations (9a) and (9b) can also be treated using FDTD methods. The natural choice is to locate the scalar field $\Psi_{0,j}$ at cell centers and evaluate it at integer time steps, whereas each of the components of the vector field $\mathbf{\Psi}_{1,j}$ is colocated with the respective component of the electric field and evaluated at semi-integer steps (Figure 1). In this scheme the update equation for $\Psi_{0,j}$ requires knowledge of the impact ionization at semi-integer time steps. We calculate this term interpolating in time the absolute value of the electric field, which is in turn calculated by interpolating each of the field components into the cell centers.

Finally, the electron density is updated using a discretized version of transport. For this purpose we implement a semi-implicit time stepping obtained from

$$\frac{n_e|^{n+1/2} - n_e|^{n-1/2}}{\Delta t} = -\nabla \cdot \Gamma_e\big|^n + S_{\text{ph}}|^n + \frac{n_e|^{n+1/2} + n_e|^{n-1/2}}{2} \nu_{\text{eff}}|^n, \tag{18}$$

where again we omit the spatial indexes (i, j) and we leave implicit the discretization of the divergence term. Note that the ionization and attachment rates are functions of the absolute value of the electric field: $\nu_{\text{eff}}|^n = \nu_{\text{eff}}(|E||^n)$. Rearranging terms, we find an update equation for the electron density:

$$n_e|^{n+1/2} = \left(1 - \frac{\nu_{\text{eff}}|^n \Delta t}{2}\right)^{-1} \left[\left(1 + \frac{\nu_{\text{eff}}|^n \Delta t}{2}\right) n_e|^{n-1/2} - \nabla \cdot \Gamma_e\big|^n \Delta t + S_{\text{ph}}|^n \Delta t\right]. \tag{19}$$

As we mentioned in section 1, our numerical scheme allows us to restrict the simulation to a narrow domain around the streamers without a significant effect. This is achieved by 32-cell-wide convolutional perfectly matched layers (Inan & Marshall, 2011) in the external boundary. In all simulations reported here the computational domain extends to about 3 cm in the radial direction, which we found was enough to accommodate our streamers. We checked that our results are unchanged with a wider domain. For the photoionization fields we apply Marshak's boundary conditions (Bourdon et al., 2007) whereas for the electron density we implement a zero-order extrapolation into two ghost cells.

In all the simulations reported here the spatial resolution is $\Delta r = \Delta z = 10$ μm and the time step $\Delta t = \Delta z/\sqrt{3}c \approx 2 \times 10^{-14}$ s. As our numerical scheme benefits from large-scale parallelization, we implemented the code in CUDA and run all simulations reported here in a Tesla K80 GPU card. The total running time was about 1 week for each simulation, and the largest one involved about 2.5×10^6 time steps of 1.7×10^8 grid points, each one containing 15 scalar fields. The code is named PESTO (Parallel Electromagnetic and Self-consistent Transport Open-source code) and is available from https://gitlab.com/aluque/PESTO. The code was verified by comparing to a previous streamer code; the results, discussed in the supporting information, confirm the correctness of our implementation.

4. Results

Let us now apply the model described above to investigate streamer collisions by setting a simulation where two streamers emerge from opposite electrodes in a plane-plane gap delimited by $z = 0$ and $z = L$. As initial conditions we simulate a protrusion-protrusion geometry starting with two capped-Gaussian ionization seeds. The lower seed has an electron density

$$n_{e,0}(r,z) = A \exp\left(-r^2/w^2 - \max(z - z_0, 0)^2/w^2\right), \tag{20}$$

with $A = 10^{21}\,\mathrm{m}^{-3}$, $w = 1$ mm, and $z_0 = 1$ cm. The upper seed is similar to the lower seed after an inversion in the z direction. We selected the radius w of the initiating seeds to be 1 mm because this approximates the typical streamer radius observed in long discharge gap experiments. The protrusion-protrusion geometry employed here overestimates the Laplacian field far from the initiation points, but this partly compensates the absence of surrounding streamers, which screen the field within the corona and uniformize the field that drives each single streamer.

Figure 2 shows the outcome of a simulation where the gap width was $L = 30$ cm, and the total potential difference between the electrodes was 750 kV, resulting in an average electric field of 25 kV/cm, below the breakdown field $E_k \approx 32$ kV/cm.

The velocity of the simulated streamers is initially around 4×10^6 m/s, in rough agreement with measurements of 2×10^6 m/s for positive streamers (Kochkin et al., 2012) and 3.7×10^6 m/s for negative streamers (Kochkin et al., 2016) under similar circumstances. However, the streamers accelerate as they approach each other, reaching 1.2×10^7 m/s in the last 5 cm of propagation. In our simulations positive streamers are faster than negative streamers, as reported in other experiments (Briels et al., 2008) and analyzed by Luque et al. (2008).

At 10 ns the electrodynamic diameter of both streamers is around 1 cm. Typically, the radiation diameter (as measured in experiments) is around half of the electrodynamic diameter so in our simulations it is around 5 mm. This is somewhat larger than the diameters shown by Kochkin et al. (2014), probably due to the streamer branching present in experiments which is absent in our deterministic simulations (the role of random fluctuations in branching processes was discussed by Luque and Ebert, 2011). As the two streamers get closer they also become wider, presumably because they experience an electric field enhanced by the opposite streamer. This increase in diameter contributes to the acceleration mentioned above, as discussed by Naidis (2009).

In Figure 2a we see the presence, just before the collision, of a high electric field between the two streamer heads, previously investigated by Ihaddadene and Celestin (2015) and Köhn et al. (2017). Since we apply a higher potential, in our simulation this field reaches around 350 kV/cm against 250 kV/cm to 300 kV/cm found by Ihaddadene and Celestin (2015) and Köhn et al. (2017).

Nevertheless, we focus here not on this field but on the field evolution during the collision. This is shown in Figure 2b, where we plot the variation of the electric field within 60 ps after the field has reached its highest value. In this brief interval we see two relevant features: an electromagnetic pulse emitted sideward and a significant electric field penetration into each of the streamer heads. Let us analyze each of these features.

4.1. Far-Field Electromagnetic Radiation

We focus first of the radiated electromagnetic pulse (EMP). This EMP originates in the strong current and quick decay of the electric field that occurs at the contact point between the two streamers. The electric field drops by a few times 100 kV/cm within about 10 ps. As the change in electric field is dominated by the z component, the radiated field is stronger in the xy plane that contains the collision point. As shown in Figure 2, according to our simulation, the field of the EMP 1 cm away from the collision is of the order of 1 kV/cm, so it is unlikely to affect neighboring streamers in a full corona, as it is significantly below the background field. Besides, as we appreciate in Figure 2, the radiated field has the opposite sign to the background field.

Nevertheless, this radiated field decays only as $1/r$ as it moves away from the collision point so it is easier to detect remotely. To investigate this, we calculated the electric field at a large horizontal distance from the collision point by means of a near-to-far-field transformation as described by (Taflove & Hagness, 2005). In this calculation we did not include the two planar electrodes which, if assumed as infinite, would produce secondary pulses. Figure 3 shows the z component of the electric field in the middle plane of our simulation and 2 m away from the central axis.

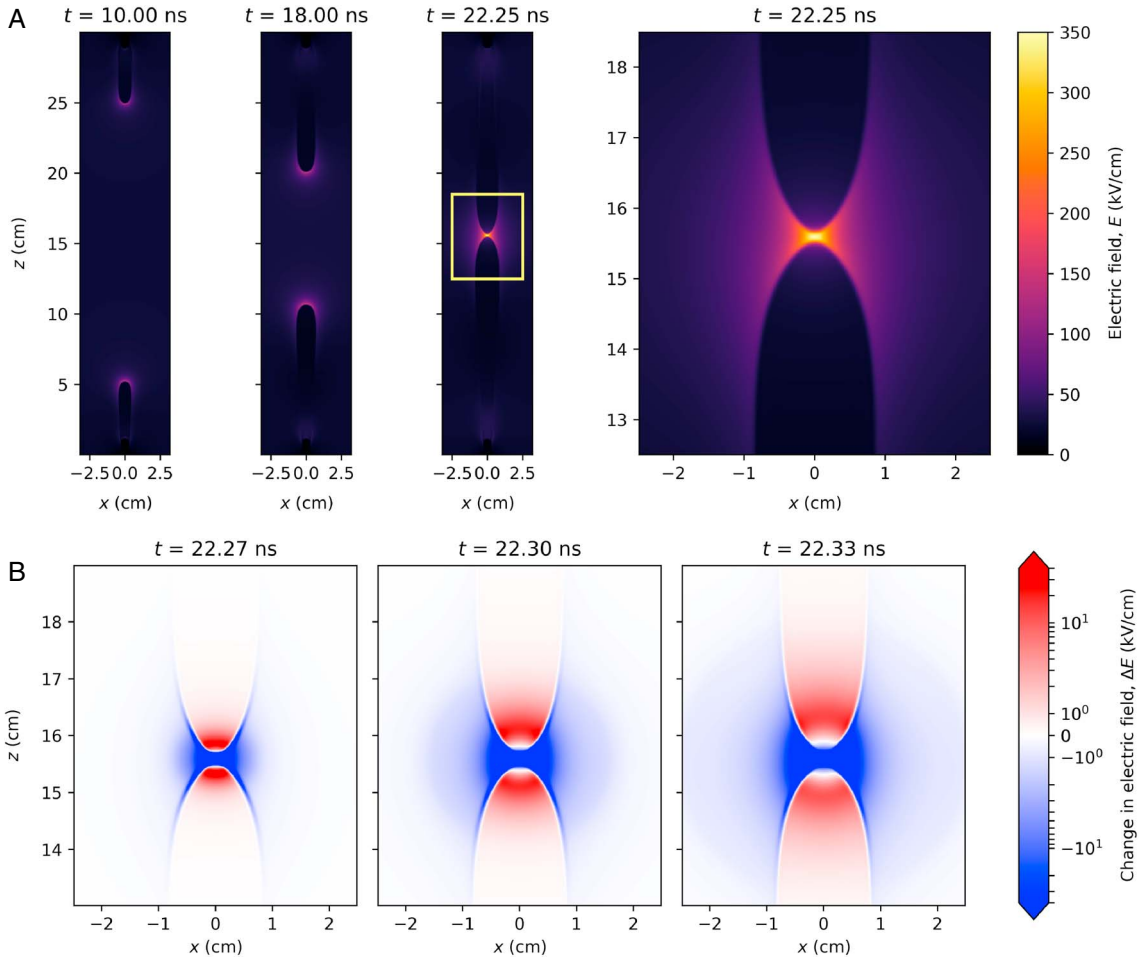

Figure 2. Simulation of a streamer encounter in a 30 cm gap under a total electrostatic potential difference of 750 kV. (a) Three snapshots of the simulation showing the electric field in the complete simulation domain. The latest snapshot (22.25 ns) contains the highest electric field of the full simulation time; a zoomed-in plot of this snapshot corresponding to the marked rectangle is shown on the left. (b) Variations in the electric field shortly after the streamer collision. Here we show the change experienced by the electric field with respect to the field at 22.25 ns (plotted above). Notice the electromagnetic pulse (a field decrease of around 1 kV/cm) as well as the increase by a few times 100 kV/cm of the field inside streamer bodies.

In the time domain plot of the electric field shown in Figure 3 (left) we see that the electromagnetic radiations from our system are dominated by the EMP emitted by the streamer collision. About 98% of the energy radiated in 50 ns of simulation is contained within a 2 ns window centered around the peak electric field.

The far-field EMP has an asymmetric bipolar shape, with a sharp negative peak (opposite to the field applied in the discharge) followed by an overshoot and a slower decay. In our simulation the initial peak reaches about 4,000 V/m and has a full width at half maximum (FWHM) of around 40 ps. The subsequent, opposite peak reaches about 300 V/m and has a FWHM of around 650 ps.

Noting that the radiated field is roughly proportional to minus the time derivative of the volume-integrated current density, we can explain the bipolar structure in Figure 3 as follows. As the gap between the streamers narrows down, the electric field between the two streamer heads increases. The resulting impact ionization quickly builds up the electron density, and this produces a rise of a discharging current which radiates the first, negative pulse. The discharge then depletes the electric field to the point where impact ionization is negligible so the further evolution is dominated by dielectric relaxation. A slower decay of the current ensues, which radiates the second, positive pulse. We emphasize that the bipolar shape of the electric field results from a single, asymmetric current pulse.

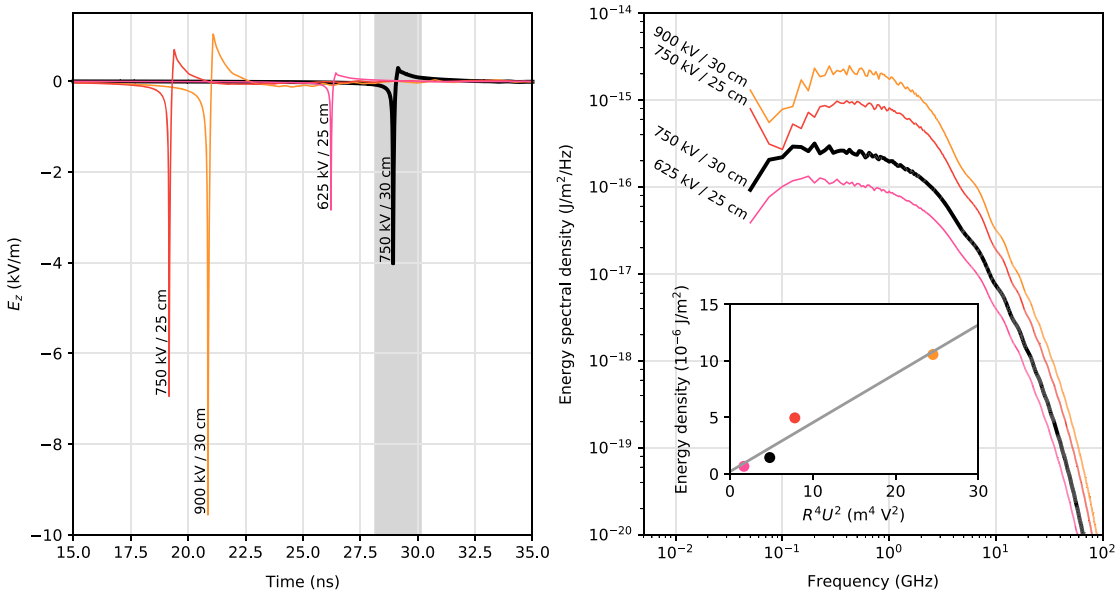

Figure 3. Vertical component of the electric field at the middle plane of the discharge and 2 m away from the central axis. (left) The time domain evolution of this field for several potential differences and gap lengths (the black thick line corresponds to the simulation in Figure 2). Note that the two streamers collide at different times in each configuration and that therefore the emitted pulses reach the detector at different times. In all cases the delay between the collision and the detection of the pulse is about 6.7 ns due to the 2 m distance from the collision point. The shaded area is a 2 ns window centered around the peak electric field: 98% of the energy radiated in 50 ns of simulation is contained in this window. (right) The spectral energy density corresponding to the time domain data in Figure 3 (left). The inset shows the scaling of the total energy that reaches the observation point as a function of R^4U^2, where R is an approximation to the streamer radius and U is the total potential between the electrodes. The solid line is a linear fit of the four data points.

The time domain electric field in Figure 3 (left) corresponds to the energy spectral density represented in Figure 3 (right). We define this quantity as $\mathcal{S} = |\tilde{E}_z(f)|^2/Z_0$, where $Z_0 = \sqrt{\mu_0/\epsilon_0}$ is the impedance of free space and $\tilde{E}_z(f)$ is the Fourier transform of the radiation electric field defined as

$$\tilde{E}_z(f) = \int_{t_0}^{t_1} E_z(t) e^{-2\pi i f t} \mathrm{d}t, \tag{21}$$

where $t_0 = 10$ ns and $t_1 = 50$ ns bound the observation interval. Assuming that the EMP propagates transversally at the observation point, $\mathcal{S}$ measures the energy per unit area and frequency that traverses this location.

We see that the spectrum peaks at around 300 MHz but is rather flat in the range 100 MHz–1 GHz and still contains significative energy around 10 GHz. The energy spectrum is dominated by the negative peak of the electric field that, although short, is more energetic, as can be explained by the following argument (provided by an anonymous referee): since the radiated field results from a single current pulse its time integral must vanish, implying $|E^+|\tau^+ \approx |E^-|\tau^-$, where $E^\pm$ and $\tau^\pm$ are the peaks and approximate durations of the positive and negative pulses. The energy contained in one pulse is proportional to the square of the electric field so the ratio between the energies in the positive and negative peaks is

$$\frac{|E^+|^2\tau^+}{|E^-|^2\tau^-} \approx \frac{|E^+|}{|E^-|}, \tag{22}$$

implying, in our case, that there is much more energy in the negative, initial peak.

To understand better the relationship between the radiated energy and the discharge characteristics, we performed three additional simulations where we changed the total potential difference between the electrodes as well as the discharge gap length. The results are plotted with thin colored lines in Figure 3 (left and right). Other things equal, a higher potential difference leads to a stronger EMP. However, comparing the two simulations with a potential difference of 750 kV, we notice that the shorter gap emits a significantly stronger pulse. The reason is that streamers are thicker when the average applied field is higher; the volume affected by the approximation of the two streamers is correspondingly larger, and this translates into a stronger pulse.

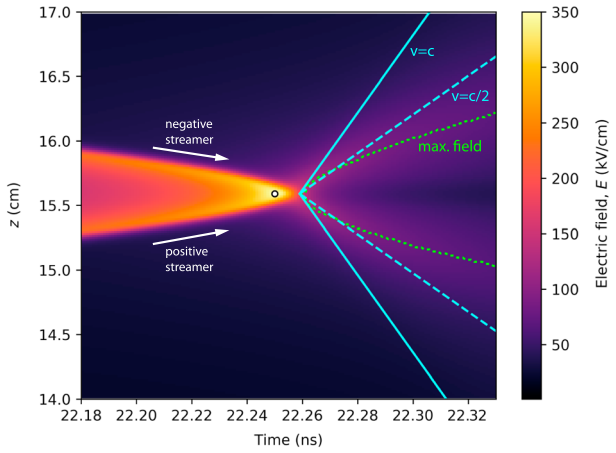

Figure 4. Electric field at the central axis around the time of the collision. The electric field created by the colliding streamers increases as the two heads approach each other. After the collision time, around 22.25 ns, the potential difference spreads within the two streamer bodies. For illustration, we have plotted a light cone initiated at the collision as well as a cone defined by a propagation speed $v = c/2$. The green dotted line follows the two maxima of the electric field along the z direction. The white dot marks the location and time of launch of a 1 keV test electron as described in the text.

Changes in the streamer diameter also explain the more-than-linear increase of the radiated energy that follows an increase of the potential difference for a fixed gap length.

We can test these relationships and make them more precise by devising a simple model for streamer collisions. Assume that (a) the discharge between the two streamers takes place when the field between them reaches a fixed field E_{max} common to all collisions and that (b) the total discharge time is also common to all configurations. Under these admittedly crude assumptions the magnitude and evolution of the local electric current density $\mathbf{J}$ are similar in all collisions. Then, as the radiated field is proportional to the integral of $\partial\mathbf{J}/\partial t$ and power is proportional to the square of this quantity, we expect the total radiated energy to be proportional to the square of the volume V bounded by the two streamer heads during the collision. But according to our assumption (a) this volume scales as $V \sim R^2U/E_{max}$, where R is the streamer radius and U is the total potential difference between the electrodes, which we assume is carried also by the streamer tips. Putting all these arguments together, we find that the total energy per collision should scale as R^4U^2. In order to test this scaling, we calculated the streamer radius as the average distance to the central axis of all electrons in the simulation at the time of the highest electric field. With this definition we produced the data plotted in the inset in Figure 3 (right), which shows that our scaling relation works reasonably well for our simulations.

A long-gap discharge or the merging of streamer coronas during the stepping of a leader contains a multitude of streamer encounters, each one emitting a pulse such as those represented in Figure 3. Assuming that the times of such encounters are uncorrelated, the total emitted spectrum results from the addition of the spectra of single pulses. Since all the spectra in Figure 3 have approximately the same shape, we expect the combined spectrum to maintain this shape, peaking around 300 MHz and extending up to a few gigahertz. In principle it should be possible to estimate the rate of streamer encounters per unit time from a measurement of the radiated power. Such an estimate, however, requires some knowledge of the streamer diameters and the potential that they carry.

4.2. Electric Field Penetration

We now turn back to Figure 2 and focus on the second feature that we mentioned above: the electric field that penetrates into each streamer head immediately after the collision.

One explanation for this electric field is as follows. The two approaching positive and negative streamers carry on their heads a corresponding charge that screens the electric field in the interior. The conduction path established by the collision neutralizes most of this charge, and as screening weakens, the field penetrates into the streamers. An alternative description is that this field originates from the potential difference between the two streamers, which immediately before the collision is squeezed within the region between them and has to be redistributed after the streamer encounter.

Figure 4 shows the evolution of the electric field on the central axis of the simulation around the collision time. The penetrating field is characterized by two bumps that diverge and spread out. The two maxima reach about 150 kV/cm, and they slow down as they propagate away from the collision point, travelling close to the speed of light initially and somewhat below half of this speed after 80 ps. Note that the field along the axis is not a radiation field but a combination of electrostatic and induction fields.

Because the velocity of electric field penetration is comparable to the speed of light, the effects of electromagnetic propagation are not negligible for this process. There is certain delay between the time of the streamer collision and its effect on electrons some distance away from it. This is relevant in calculations of the decay properties of the penetrating fields, particularly within a few tens of picoseconds after the collision.

5. Implications for High-Energy Emissions

Our results have some bearing on the topic of X-ray emissions from lightning leaders and long electrical discharges. First, our model predicts the amplitude and spectrum of the radio emissions from the streamer collisions where electrons may be accelerated. As we discussed above, the amplitude of the emissions depends strongly on properties of the colliding streamers, such as their radius. Therefore, a very good characterization of the discharge is required in order to derive information from amplitude measurements.

On the other hand, the overall shape of the spectra plotted in Figure 3 is largely independent of the discharge properties. Our simulations predict that the radiation in the UHF range (300 MHz – 3 GHz) emitted by streamers is dominated by the EMP radiated from the collision. Therefore, the correlation between X-ray and UHF signals reported by Montanyà et al. (2015) adds support to the hypothesis that streamer collisions are necessary for the acceleration of electrons above 1 keV energies.

In this work we did not investigate this electron acceleration but we note that by considering a much larger gap and a significantly higher potential difference than the works of Ihaddadene and Celestin (2015) and Köhn et al. (2017), our simulations predict a larger volume where the electric field is above the threshold for cold runaway. Likely, this results in more electrons accelerated above 1 keV. However, it is currently unclear if this would be enough to explain the observed X-ray fluences.

We also draw attention to the penetration of electric fields inside the streamer. If an electron is accelerated beyond the runaway threshold during the collision, it will pass through these fields and gain additional energy. To investigate the extent of this acceleration, we simulated the average dynamics of an electron that starts at the central axis with an energy of 1 keV and moves downward. The average here means that the electron, while accelerated by the electric field from the simulation, experiences a deterministic friction given by the stopping power of air (we took the expressions from the supporting information of Luque (2014)). In our simulation the electron gains about 5 keV in the few millimeters between the streamer heads and about 100 keV within the approximately 2 cm where the electric fields penetrate into the streamer. Carlson et al. (2015) estimate the average energy of runaway electrons in high-voltage discharges as 200 keV to 400 keV, a result that was later refined by Østgaard et al. (2016) with the direct detection of electrons with around 300 keV, so we hypothesize that a significant fraction of this energy is provided by the penetrating fields. Bringing the electron energy to around 100 keV is important because at those energies the stopping power of air is significantly lower than at energies around 1 keV so after reaching 100 keV an electron, even in a relatively weak electric field, can be possibly accelerated to the 300 keV estimated by Østgaard et al. (2016).

5.1. Conclusion

The characteristic time of a streamer discharge at atmospheric pressure is around 1 ns and light travels 30 cm in this time. Since this distance is larger than the characteristic size of a streamer, the quasi-static approximation is justified in most situations involving streamer discharges. A head-on collision between streamers is an exception because it involves such short time scales that the wavelength of the corresponding radiation is not much larger than the characteristic system size. In those cases the quasi-static approximation breaks down and a full electromagnetic model is required. Here we described a practical implementation of such a model and applied it to investigate streamer encounters.

With our electromagnetic model we characterized high-frequency radio emissions from streamer collisions in long-gap discharges. Besides laboratory discharges, streamer-related high-frequency emissions are also emitted during leader progression (Petersen & Beasley, 2014), and we speculate that they are in large part generated during the collisions between streamers connected to the main leader channel and streamers emerging from a space stem. Similarly, in high-altitude discharges (sprites) positive streamers collide with negative streamers launched from persisting glows (Luque et al., 2016) or beads (Luque & Gordillo-Vázquez, 2011) and these collisions possibly emit radiation that, due to density scaling, concentrates on frequencies around 4 kHz.

We also mention the high-frequency radiation from other processes such as fast positive breakdown (FPB) (Rison et al., 2016), which may be a common precursor of all lightning discharges but that we still understand only partially. It is, for example, not known if only positive streamers are involved in FPB or if counter-propagating negative streamers are also present. We hope that our model, by linking remote high-frequency electric field measurements with the microphysics of streamers, will help in clarifying issues like this one.

Finally, as discussed in section 5, our results impinge on the topic of X-ray emissions from electric discharges. Our simulations show that short-lived electric fields that penetrate the streamer body after the collision are enough to accelerate electrons up to around 100 keV, which is presumed to be the typical energy of X-ray-producing electrons in a laboratory discharge.

The topics that we touched in this paper deserve further study. Perhaps some of the pending questions in high-energy atmospheric physics (Dwyer et al., 2012) will be elucidated by more complete models that couple relativistic particles with electromagnetic wave propagation. The work presented here aims to be one of the two legs of such constructions.

Acknowledgments
We acknowledge one anonymous referee for providing the argument in section 4.1 that explains that there is more energy in the first peak of the radiated field. This work was supported by the European Research Council (ERC) under the European Union H2020 programme/ERC grant agreement 681257 and by the Spanish Ministry of Science and Innovation, MINECO under projects FIS2014-61774-EXP and ESP2015-69909-C5-2-R. The full source of the code described here is available at https://gitlab.com/aluque/PESTO. Input files are provided as supporting information. The full output data of the simulations reported here can be requested from the author (aluque@iaa.es).

References

Berenger, J.-P. (1994). A perfectly matched layer for the absorption of electromagnetic waves. *Journal of Computational Physics*, *114*, 185–200. https://doi.org/10.1006/jcph.1994.1159

Bourdon, A., Pasko, V. P., Liu, N. Y., Célestin, S., Ségur, P., & Marode, E. (2007). Efficient models for photoionization produced by non-thermal gas discharges in air based on radiative transfer and the Helmholtz equations. *Plasma Sources Science and Technology*, *16*, 656–678. https://doi.org/10.1088/0963-0252/16/3/026

Briels, T. M. P., Kos, J., Winands, G. J. J., van Veldhuizen, E. M., & Ebert, U. (2008). Positive and negative streamers in ambient air: Measuring diameter, velocity and dissipated energy. *Journal of Physics D*, *41*(23), 234004. https://doi.org/10.1088/0022-3727/41/23/234004

Carlson, B. E., Østgaard, N., Kochkin, P., Grondahl, Å., Nisi, R., Weber, K., … LeCaptain, K. (2015). Meter-scale spark X-ray spectrum statistics. *Journal of Geophysical Research: Atmospheres*, *120*, 11,191–11,202. https://doi.org/10.1002/2015JD023849

Cooray, V., Arevalo, L., Rahman, M., Dwyer, J., & Rassoul, H. (2009). On the possible origin of X-rays in long laboratory sparks. *Journal of Atmospheric and Solar-Terrestrial Physics*, *71*, 1890–1898. https://doi.org/10.1016/j.jastp.2009.07.010

Davies, A. J., Davies, C., & Evans, C. (1971). Computer simulation of rapidly developing gaseous discharges. *Proceedings of the Institution of Electrical Engineers*, *118*(6), 816–823. https://doi.org/10.1049/piee.1971.0161

Dwyer, J. R., Rassoul, H. K., Saleh, Z., Uman, M. A., Jerauld, J., & Plumer, J. A. (2005). X-ray bursts produced by laboratory sparks in air. *Geophysical Research Letters*, *32*, L20809. https://doi.org/10.1029/2005GL024027

Dwyer, J. R., Schaal, M., Rassoul, H. K., Uman, M. A., Jordan, D. M., & Hill, D. (2011). High-speed X-ray images of triggered lightning dart leaders. *Journal of Geophysical Research*, *116*, D20208. https://doi.org/10.1029/2011JD015973

Dwyer, J. R., Smith, D. M., & Cummer, S. A. (2012). High-energy atmospheric physics: Terrestrial gamma-ray flashes and related phenomena. *Space Science Reviews*, *173*, 133–196. https://doi.org/10.1007/s11214-012-9894-0

Ihaddadene, M. A., & Celestin, S. (2015). Increase of the electric field in head-on collisions between negative and positive streamers. *Geophysical Research Letters*, *42*, 5644–5651. https://doi.org/10.1002/2015GL064623

Inan, U., & Marshall, R. (2011). *Numerical Electromagnetics: The FDTD Method*. Cambridge, UK: Cambridge University Press.

Kochkin, P., Lehtinen, N., Deursen, A. P. J., & Østgaard, N. (2016). Pilot system development in metre-scale laboratory discharge. *Journal of Physics D*, *49*, 425,203. https://doi.org/10.1088/0022-3727/49/42/425203

Kochkin, P. O., Nguyen, C. V., van Deursen, A. P. J., & Ebert, U. (2012). Experimental study of hard X-rays emitted from metre-scale positive discharges in air. *Journal of Physics D*, *45*, 425,202. https: //doi.org/10.1088/0022-3727/45/42/425202

Kochkin, P. O., van Deursen, A. P. J., & Ebert, U. (2014). Experimental study of the spatio-temporal development of metre-scale negative discharge in air. *Journal of Physics D*, *47*(14), 145,203. https://doi.org/10.1088/0022-3727/47/14/145203

Kochkin, P. O., van Deursen, A. P. J., & Ebert, U. (2015). Experimental study on hard X-rays emitted from metre-scale negative discharges in air. *Journal of Physics D*, *48*(2), 25,205. https://doi.org/10.1088/0022-3727/48/2/025205

Köhn, C., Chanrion, O., & Neubert, T. (2017). Electron acceleration during streamer collisions in air. *Geophysical Research Letters*, *44*, 2604–2613. https://doi.org/10.1002/2016GL072216

Legler, W. (1963). Anregung von UV-strahlung in Stickstoff und Wasserstoff durch einen Elektronenschwarm. *Zeitschrift für Physik*, *173*, 169–183.

Luque, A. (2014). Relativistic runaway ionization fronts. *Physical Review Letters*, *112*(4), 45,003. https: //doi.org/10.1103/PhysRevLett.112.045003

Luque, A., & Ebert, U. (2009). Emergence of sprite streamers from screening-ionization waves in the lower ionosphere. *Nature Geoscience*, *2*, 757–760. https://doi.org/10.1038/ngeo662

Luque, A., & Ebert, U. (2011). Electron density fluctuations accelerate the branching of positive streamer discharges in air. *Physical Review E*, *84*(4), 46411. https://doi.org/10.1103/PhysRevE.84.046411

Luque, A., & Gordillo-Vázquez, F. J. (2011). Sprite beads originating from inhomogeneities in the mesospheric electron density. *Geophysical Research Letters*, *38*, L04808. https://doi.org/10.1029/2010GL046403

Luque, A., Ebert, U., Montijn, C., & Hundsdorfer, W. (2007). Photoionization in negative streamers: Fast computations and two propagation modes. *Applied Physics Letters*, *90*(8), 81501. https://doi.org/10.1063/1.2435934

Luque, A., Ratushnaya, V., & Ebert, U. (2008). Positive and negative streamers in ambient air: Modelling evolution and velocities. *Journal of Physics D*, *41*(23), 234005. https://doi.org/10.1088/0022-3727/41/23/234005

Luque, A., Stenbaek-Nielsen, H. C., McHarg, M. G., & Haaland, R. K. (2016). Sprite beads and glows arising from the attachment instability in streamer channels. *Journal of Geophysical Research: Space Physics*, *121*, 2431–2449. https://doi.org/10.1002/2015JA022234

Malagón-Romero, A., & Luque, A. (2017). A domain-decomposition method to implement electrostatic free boundary conditions in electric discharges. arXiv:1708.09444.

Montanyà, J., Fabró, F., March, V., van der Velde, O., Solà, G., Romero, D., & Argemí, O. (2015). X-rays and microwave RF power from high voltage laboratory sparks. *Journal of Atmospheric and Solar-Terrestrial Physics*, *136*, 94–97. https://doi.org/10.1016/j.jastp.2015.06.009

Montijn, C., Hundsdorfer, W., & Ebert, U. (2006). An adaptive grid refinement strategy for the simulation of negative streamers. *Journal of Computational Physics*, *219*, 801–835. https://doi.org/10.1016/j.jcp.2006.04.017

Moore, C. B., Eack, K. B., Aulich, G. D., & Rison, W. (2001). Energetic radiation associated with lightning stepped-leaders. *Geophysical Research Letters*, *28*, 2141–2144. https://doi.org/10.1029/2001GL013140

Moss, G. D., Pasko, V. P., Liu, N., & Veronis, G. (2006). Monte Carlo model for analysis of thermal runaway electrons in streamer tips in transient luminous events and streamer zones of lightning leaders. *Journal of Geophysical Research*, *111*, A02307. https://doi.org/10.1029/2005JA011350

Naidis, G. V. (2009). Positive and negative streamers in air: Velocity-diameter relation. *Physical Review E*, *79*(5), 57401. https://doi.org/10.1103/PhysRevE.79.057401

Nguyen, C. V., van Deursen, A. P. J., & Ebert, U. (2008). Multiple X-ray bursts from long discharges in air. *Journal of Physics D*, *41*(23), 234012. https://doi.org/10.1088/0022-3727/41/23/234012

Nguyen, C. V., van Deursen, A. P. J., van Heesch, E. J. M., Winands, G. J. J., & Pemen, A. J. M. (2010). X-ray emission in streamer-corona plasma. *Journal of Physics D*, *43*(2), 25202. https://doi.org/10.1088/0022-3727/43/2/025202

Østgaard, N., Carlson, B. E., Nisi, R. S., Gjesteland, T., Grøndahl, Ø., Skeltved, A., … Kochkin, P. (2016). Relativistic electrons from sparks in the laboratory. *Journal of Geophysical Research: Atmospheres*, *121*, 2939–2954. https://doi.org/10.1002/2015JD024394

Petersen, D., & Beasley, W. (2014). Microwave radio emissions of negative cloud-to-ground lightning flashes. *Atmospheric Research*, *135*, 314–321. https://doi.org/10.1016/j.atmosres.2013.02.006

Rahman, M., Cooray, V., Azlinda Ahmad, N., Nyberg, J., Rakov, V. A., & Sharma, S. (2008). X rays from 80-cm long sparks in air. *Geophysical Research Letters*, *35*, L06805. https://doi.org/10.1029/2007GL032678

Rison, W., Krehbiel, P. R., Stock, M. G., Edens, H. E., Shao, X.-M., Thomas, R. J., … Zhang, Y. (2016). Observations of narrow bipolar events reveal how lightning is initiated in thunderstorms. *Nature Communications*, *7*, 10721. https://doi.org/10.1038/ncomms10721

Ségur, P., Bourdon, A., Marode, E., Bessieres, D., & Paillol, J. H. (2006). The use of an improved Eddington approximation to facilitate the calculation of photoionization in streamer discharges. *Plasma Sources Science and Technology*, *15*, 648–660. https://doi.org/10.1088/0963-0252/15/4/009

Taflove, A., & Hagness, S. (2005). *Computational electrodynamics: The finite-difference time-domain method*, Artech House antennas and propagation library, pp. 2005. Norwood, MA: Artech House.

Teunissen, J., & Ebert, U. (2017). Afivo: A framework for quadtree/octree AMR with shared-memory parallelization and geometric multigrid methods.

Wormeester, G., Pancheshnyi, S., Luque, A., Nijdam, S., & Ebert, U. (2010). Probing photo-ionization: Simulations of positive streamers in varying N_2: O_2-mixtures. *Journal of Physics D*, *43*, 505201. https://doi.org/10.1088/0022-3727/43/50/505201

Yee, K. (1966). Numerical solution of initial boundary value problems involving Maxwell's equations in isotropic media. *IEEE Transactions on Antennas and Propagation*, *14*(3), 302–307. https://doi.org/10.1109/TAP.1966.1138693

Zhelezniak, M. B., Mnatsakanian, A. K., & Sizykh, S. V. (1982). Photoionization of nitrogen and oxygen mixtures by radiation from a gas discharge. *Teplofizika Vysokikh Temperatur*, *20*, 423–428.